A CDL-Based Channel Model With Dual-Polarized Antennas for 5G MIMO Systems in Rural Remote Areas

ALEXANDRE MATOS PESSOA[ID], (Student Member, IEEE),
BRUNO SOKAL[ID], (Student Member, IEEE), **CARLOS F. M. E SILVA**[ID], (Member, IEEE),
TARCISIO FERREIRA MACIEL[ID], **ANDRÉ L. F. DE ALMEIDA**[ID], (Senior Member, IEEE),
AND FRANCISCO RODRIGO PORTO CAVALCANTI, (Member, IEEE)

Wireless Telecom Research Group (GTEL), Federal University of Ceará (UFC), Fortaleza 60440-900, Brazil

Corresponding author: Alexandre Matos Pessoa (alexandrematos@gtel.ufc.br)

ABSTRACT In the fifth-generation (5G) mobile networks, it is expected that users experience high throughputs with an ultra-low-latency network, while a massive number of devices are connected to the network. However, in remote rural areas, there is still a large number of people that do not have access to broadband Internet. To overcome this issue, a possible strategy is to exploit the excellent propagation conditions of very high frequency (VHF) and ultra-high frequency (UHF) bands by allowing secondary spectrum reuse in the TV white space (TVWS) channels. But for that, a reliable channel model is required to perform valid coverage and data rate prediction studies. In this paper, a channel model is proposed that takes into account large and small scale fading effects, as well as the particularities of such remote rural areas. The proposed model makes use of measurements along with the clustered delay line (CDL) profiles from 3rd Generation Partnership Project (3GPP). It is a simple model to implement and can be used to provide fast link and system-level simulations. Numerical and analytical results are provided to validate the proposed model and a data rate evaluation is carried out for single-input single-output (SISO) and multiple-input multiple-output (MIMO) configurations, as well as for single-polarized (SP) and dual-polarized (DP) antennas.

INDEX TERMS Channel modeling, remote rural areas, CDL, MIMO and dual-polarized antennas.

I. INTRODUCTION

It is well known that mobile users demand higher throughputs and better quality of service (QoS) every year. A study conducted by Qualcomm and Nokia [1] shows that since 2014 the mobile traffic is almost doubling every year. The next generation of mobile networks, 5G, needs not only to attend this demand for smartphones, but also bring to the society a new experience, where "everything" is connected. The 5G mobile networks use cases can be classified into three categories, according to the International Telecommu-

nication Union (ITU) [2]: the enhanced mobile broadband (eMBB) which consists in services that demand a high bandwidth, such as videos in ultra-high definition (UHD); the ultra-reliable low latency communications (uRLLC) which includes services that are sensitive to latency and delay, such as remote surgery, self-driving cars; and the massive machine-type communications (mMTC), where a massive number of devices are connected, bringing the concept of smart cities and Internet of Things (IoT). However, these new experiences are usually projected for urban areas.

In this manner, one may think that the deployment and operational costs [3] of 5G mobile networks in rural areas are not profitable (costs *vs.* incomes) and, therefore, do not

The associate editor coordinating the review of this manuscript and approving it for publication was Jiayi Zhang[ID].

attract investments from operators [4], since, compared to urban areas, have a lower user density. With the lack of investment in rural/remote areas, the number of unconnected people is still large, which is a serious drawback for the digital inclusion and that limits the democracy in accessing to mobile services and information. In [5], the authors discuss strategies to be employed in rural and remote areas to provide broadband access.

To overcome the possible high costs of these networks in rural areas, some alternatives may be employed. For example, the virtualization of the network or some nodes, using the software-defined network (SDN) and network function virtualization (NFV) concepts, in order to have, e.g., a cloud-radio access network (C-RAN) [6], [7]; use new sources of renewable energy and efficient solutions that switch-off the base station (BS) when there is no data traffic; and exploit the excellent propagation conditions of VHF and UHF bands by enabling the spectrum sharing in TVWS channels [8], so that secondary users reuse the licensed spectrum from primary users, without causing harmful interference to the latter ones (namely, television (TV) broadcasters) [9].

In November 2017, a partnership project between Europe and Brazil, called Remote area Access Network for 5th GEneration (5G-RANGE), was started, aiming to meet the broadband Internet demands in remote rural areas. The 5G-RANGE project adopts the TVWS strategy, which not only significantly reduces the deployment and operational costs (secondary use), but also makes it possible for the network to cover a wider area with fewer BSs due to the lower signal attenuation in the VHF and UHF bands. For this network design, the channel characterization is of utmost importance, since it allows operators to perform valid coverage and data rate prediction studies.

The project specification considers a single cell with radius (coverage) up to 50 km and frequency ranges from 170 MHz to 400 MHz and from 450 MHz to 700 MHz (VHF and UHF). The bandwidth of each TVWS channel is 6 MHz in Brazil, while in Europe it is 8 MHz. More details can be found in the first 5G-RANGE report on application and requirements [10].

In this paper, it is proposed a CDL-based channel model for 5G MIMO systems in remote rural areas with support for SP and DP antennas, wherein the large and small scale fading parameters are based on measurements performed by Telstra and Ericsson [11] and in the rescaled values of CDL-A and CDL-D models of 3GPP standards [12], respectively. The model is simple to be implemented and may be used in both link and system-level simulations.

In order to validate the implementation of the proposed channel model, its autocorrelation function (ACF) is analytically derived and compared with numerical simulations. The results also include an analysis of the channel eigenvalues and the evaluation of the achievable data rate when the user equipment (UE) is in the cell-edge considering SISO and MIMO (2×2 and 4×4) configurations. In fact, this work is an extension of [13], whereas the main differences are listed below:

1) The CDL-D model has been added, which covers scenarios with a dominant line-of-sight (LOS) component;
2) The channel generation and the rescaling procedures for both CDL models from 3GPP have been extended and are presented with more details;
3) An analytical derivation of the ACF of the proposed channel model is provided for both CDL models. Besides obtaining an analytical result for the coherence time and coherence bandwidth, this result was used to calibrate the model by comparing the closed-form expression for the channel ACF with the one obtained by numerical simulations;
4) The new achievable data rate study takes into account DP antennas. Moreover, for the MIMO case, a study of the channel eigenvalues using the eigenvalue decomposition (EVD) is carried out considering both CDL-A and CDL-D models.

The rest of the paper is organized as follows: section II presents a brief literature review, wherein section II-A discusses rural channel models for 5G networks, as well as a measurement campaign in [11], and section II-B discusses the benefits of employing DP antennas and possible scenarios that would benefit from it. In section III, the proposed large and small scale fading models are presented, which characterize the channel for the 5G-RANGE project; channel analysis and performance simulations are done and discussed in section IV. Finally, in section V the conclusions are drawn.

II. LITERATURE REVIEW
As mentioned in section I, 5G networks will provide a new experience to users in terms of connectivity. In this context, the channel characterization for different scenarios and applications is a very important task. In the literature, several works have been proposed for channel modeling in different applications. In a specific scenario, e.g., the works of [18], [19] propose different channel models for vehicular-to-vehicular communications in 5G networks. Nevertheless, for more general scenarios such as indoor/outdoor in a urban/rural environment, there are many channel models proposed based on measurement campaigns such as 3GPP [12], International Mobile Telecommunications (IMT)-2020 [14], Quasi Deterministic Radio channel Generator (QuaDRiGa) [16], Millimetre-Wave Based Mobile Radio Access Network for Fifth Generation Integrated Communications (mmMAGIC) [20], Mobile and wireless communications Enablers for the Twenty-twenty Information Society (METIS) 2020 [21]. The work of [22] compiles a complete survey over these models.

However, for the context of the present work, it is given attention to channel modeling for remote rural areas. A closer look at this topic is briefly taken in the following section, where the applicability of DP antennas is also discussed.

TABLE 1. Specifications of channel models for rural areas.

	3GPP [12]	IMT-2020 [14]	WINNER II [15]	QuaDRiGa [16]	COST 259 [17]	Proposed
Max. distance (km)	10	21	10	10	20	50
f_c (GHz)	0.5–7	0.5–30	2–6	0.5–100	0.15–2	VHF and UHF
Bandwidth (MHz)	10% of f_c	100	100	1000	5	24
Support for MIMO	yes	yes	yes	yes	no	yes (up to 4×4)
Support for cross-pol. antennas	yes	yes	yes	yes	yes	yes
3D model	yes	yes	yes	yes	yes	yes
Computational complexity[a]	high	high	medium	high	low	low

[a] The models [12], [14], [16] demand a larger complexity because they support double-directional antennas modeling, mobility with smooth time evolution, and also capture the spatial correlation of the channel parameters for nearly located UEs. The model [15] also includes the spatial correlation of the channel parameters during the UE drop but presents a simplified mobility model. Finally, the models [17] and the proposed one present a simplified mobility and no spatial correlation during the UE drop, which justifies their smaller complexity.

A. RURAL CHANNEL MODELS

Rural areas are usually characterized by high effective BS heights, small cities with few buildings, or farms, natural scatterers and low density of users [4]. In the literature related to 5G mobile networks, Wireless World Initiative New Radio (WINNER) II [15], QuaDRiGa [16], and 3GPP TR 38.901 [12] can be cited as geometric-stochastic channel models (GSCMs) that account for rural macro (RMa) areas. In table 1 some specifications of these channels are shown. However, none of these models can be directly applied in the 5G-RANGE project, due to coverage and/or carrier frequency f_c limitations.

As previously mentioned, in [11] a measurement campaign was performed by Telstra and Ericsson for remote rural areas on third generation (3G) live cells (band 5: 850 MHz), with distances up to 200 km. The path loss and the root-mean-square (RMS) delay spread (DS) were measured using connected UE over 50 cells in four different scenarios, with 500 m to 600 m as the relative height difference between the BS and the UE. Based on these measurements, a path loss model is proposed in [23] for the remote rural areas as:

$$\mathrm{PL}(d, f_c) = \mathrm{FSPL}(d, f_c) + K, \qquad (1)$$

where $\mathrm{FSPL}(d, f_c) = 32.45 + 20 \log_{10}(d) + 20 \log_{10}(f_c)$ is the free space path loss (FSPL) at distance d in km for a carrier frequency f_c in MHz, and K is an offset in dB. The values of the offset K and shadowing that the authors have recommended are in table 2.

TABLE 2. Offset and shadowing values for the FSPL model.

	Offset (dB)	Shadowing std. (dB)	Range (km)
Ref. [23]	20	8	45–115
Proposed	29.38	4.47	1–50

It is important to mention that in [11], the authors considered as distance of interest the range between 45 and 115 km in order to predict the value of offset K in (1). Moreover, it is well known that in the literature there are many models that could be applied to a large range of frequencies and distances, such as the Longley & Rice model [24], ITU-P-1546 [25], and the Hata-Davidson model [26]. Nevertheless, the authors

in [23] argue that the path loss in (1) is simpler than the other models and shows a good agreement with the measurement data.

Using the measurements from [11], the authors of [27] have used the CDL-A from [12], which is valid for the non-line-of-sight (NLOS) case, to model the fast fading in link-level and system-level simulations. Therein, it was concluded that the RMS delay spread does not change as function of the distance and, due to the long distance and high effective antenna height, a small angular spread is expected.

B. APPLICATION OF DUAL-POLARIZED ANTENNAS

The use of DP antennas to achieve a higher diversity or multiplexing gain in MIMO systems is not new. In [28], a performance evaluation comparing the Alamouti orthogonal space-time block (OSTBC) with uncoded spatial multiplexing is done. In [29], a channel model for DP MIMO system with channel capacity evaluations is proposed. Other works addressing the performance of polarized MIMO channels can be found, for instance, in [30] and [31].

For 5G mobile networks, where the transmitter and the receiver may be equipped with antenna arrays that have a massive number of antenna elements, the physical spacing between those elements is crucial. For these networks, in [32] the authors propose a DP MIMO channel model for massive MIMO systems in the context of human-care IoT devices, while in [33], the authors propose a beamforming scheme by exploiting the DP diversity in 5G millimeter wave (mmW) systems.

Now, taking into account lower frequencies (VHF and UHF bands), due to the required space separation between the antenna elements in the array (usually, $\lambda_c/2$, and $\lambda_c \propto 1/f_c$),[1] there is a physical limitation in the number of antennas at the transmitter and receiver (especially at the UE) and, consequently, in the channel capacity gain. In this case, the use of DP antennas, both at the transmit and receive, virtually increases the array size by a factor of four. Thus, a SISO configuration with DP antennas is actually a virtual 2×2 MIMO, since the antenna array has two feeders, one for each

---

[1]Note that, λ_c and f_c are the carrier wavelength and frequency, respectively.

polarization. Nevertheless, this case will be denoted as DP SISO in the remainder of this paper.

III. PROPOSED CHANNEL MODEL

This section details the proposed channel model derivation: the large and small scale fading, and the channel model generation procedure.

A. LARGE SCALE FADING

As in [23], the path loss model in (1) is here adopted due to its simplicity. However, the value of K, in this case, is computed from the measurement data of the four different scenarios in [11] as illustrated in figure 1, covering only the distance of interest, i.e., 1 km to 50 km. For this purpose, the unconstrained minimum mean squared error (MMSE) method is used in this work, which is given by:

$$\min_{K} \left\{ f(K) = \frac{1}{I} \sum_{i=1}^{I} (e(d_i))^2 \right\}, \qquad (2)$$

where $I = 191$ is the number of measured points in figure 1 and $e(d_i) = \mathrm{PL}(d_i, f_c) - y(d_i)$ is the error between the measured point $y(d_i)$, which is an average of thousands of samples to remove the fast fading fluctuations, and the proposed path loss model in (1). Thus, differentiating (2) with respect to K and equaling it to zero yields:

$$K = \frac{1}{I} \sum_{i=1}^{I} (y(d_i) - \mathrm{FSPL}(d_i, f_c)) = 29.38 \, \mathrm{dB}, \qquad (3)$$

which is the unique optimal solution of (2) since it is a convex function in K.

The extraction of the shadowing is done by subtracting the measured data from the proposed path loss, i.e., $\mathrm{SF}(d_i) = y(d_i) - \mathrm{PL}(d_i, f_c)$. But, since the distribution of the shadowing (SF) is unknown, its histogram is plotted, as shown in figure 2, where the number of bins is calculated following a simple rule $k_{\mathrm{bin}} = \lceil \sqrt{171} \rceil$ ($I = 171$ is the number of measured points after removing the outliers). As it can be seen, the tendency is to follow a normal distribution. In fact, it is what shows the empirical probability density function (PDF) of the $\mathrm{SF}(d_i)$, obtained from the kernel smoothing method [34], and the PDF of a normal distributed random variable $\mathcal{N}(\mu_{\mathrm{SF}}, \sigma_{\mathrm{SF}}^2)$ with $\mu_{\mathrm{SF}} = \mathrm{avg}\{\mathrm{SF}(d_1), \ldots, \mathrm{SF}(d_I)\} = 0 \, \mathrm{dB}$ and $\sigma_{\mathrm{SF}} = \mathrm{std}\{\mathrm{SF}(d_1), \ldots, \mathrm{SF}(d_I)\} = 4.47 \, \mathrm{dB}$, where $\mathrm{avg}\{\cdot\}$ and $\mathrm{std}\{\cdot\}$ denote the average and standard deviation operators, respectively. As shown in figure 2, there is a good agreement between the empirical and theoretical results.

Aiming to validate the proposed SF and path loss models, it was performed a random drop of 10 000 UEs uniformly distributed in the cell area, i.e., the distance between the BS and UEs ranges from 1 km to 50 km. Next, for each UE, it was computed the path loss in (1) which is combined with a random $\mathrm{SF} \sim \mathcal{N}(0, 4.47^2)$ to provide the overall loss. figure 3 shows the cumulative distribution functions (CDFs) of the measurements in figure 1 and the overall loss obtained by simulation. From this figure, it is noted that the proposed
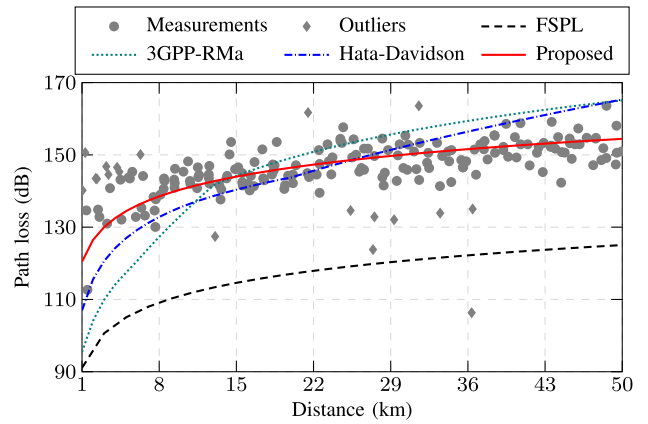
FIGURE 1. Proposed path loss model and measurements from [11]. Due to the low statistical relevance, the measured points plotted as diamonds (outliers) were removed to derive the proposed path loss and shadowing. Moreover, the 3GPP-RMa for NLOS [12] and the Hata-Davidson [26] path loss models are also presented, showing that both models do not fit well the measurements.
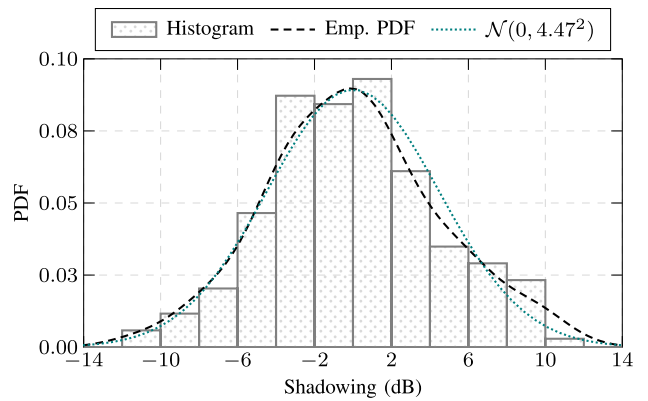
FIGURE 2. Empirical and theoretical PDFs of the estimated SF from the measurements in figure 1.
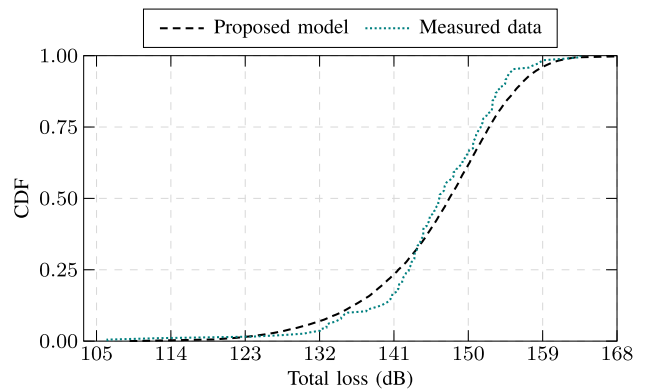
FIGURE 3. CDF of the overall propagation loss for the measurements in figure 1 and the proposed PL and SF.

path loss and SF models have a good agreement with the measurements. Finally, the values of the proposed offset K and shadowing standard deviation σ_{SF} are summarized in table 2.

B. SMALL SCALE FADING

The general channel impulse response for the proposed channel model in remote rural areas considering both LOS and NLOS conditions is given by [12], [35]:

$$
h_{u,s}(t, \tau) = \sqrt{\frac{K_R}{1+K_R}} \mathbf{f}_{UE,u,0}^T \mathbf{X}_0 \mathbf{f}_{BS,s,0} d_{UE,0}(t) \delta(\tau-\tau_0)
$$
$$
+ \sqrt{\frac{1}{1+K_R}} \sum_{n=1}^{N} \sum_{m=1}^{M} \left(\sqrt{\frac{P_n}{M}} \mathbf{f}_{UE,u,n,m}^T \mathbf{X}_{n,m} \mathbf{f}_{BS,s,n,m} \right.
$$
$$
\left. \times d_{UE,n,m}(t) \delta(\tau-\tau_n) \right), \quad (4)
$$

where u is the antenna element index of the UE, s is the antenna element index of the BS, K_R is the Ricean K-factor, N is the number of clusters and M is the number of rays per cluster. P_n/M and τ_n denote the power and delay of each ray within the cluster n, respectively. $\mathbf{f}_{UE,u,n,m}$ and $\mathbf{f}_{BS,s,n,m}$ denote the antenna element response of the elements u and s, respectively, considering the ray m within the cluster n. For the single LOS ray the antenna gains of the transmitter and receiver are denoted by $\mathbf{f}_{BS,s,0}$ and $\mathbf{f}_{UE,u,0}$, respectively. In this context, the expression for $\mathbf{f}_{BS,s,n,m}$ is given by:

$$
\mathbf{f}_{BS,s,n,m} = \sqrt{\Psi_s(\theta_{n,m}^{ZOD}, \phi_{n,m}^{AOD})} \begin{bmatrix} \cos(\xi_s) \\ \sin(\xi_s) \end{bmatrix}
$$
$$
\times \exp\left(\frac{2\pi j}{\lambda} \mathbf{r}^T(\theta_{n,m}^{ZOD}, \phi_{n,m}^{AOD}) \mathbf{d}_s \right), \quad (5)
$$

where Ψ_s denotes the radiation power pattern of the antenna element s, $\theta_{n,m}^{ZOD}$ and $\phi_{n,m}^{AOD}$ are the zenith angle of departure (ZOD) and azimuth angle of departure (AOD) of ray m within the cluster n, respectively. λ is the wavelength, $\xi_s \in [-45°, 0°, 45°, 90°]$ is the polarization angle of the antenna element s which considers single-linear and cross-linear polarization (for details see [12], section 7.3.2, model 2), $\mathbf{r}^T(\theta_{n,m}^{ZOD}, \phi_{n,m}^{AOD})$ represents the pair of angles $(\theta_{n,m}^{ZOD}, \phi_{n,m}^{AOD})$ in the Cartesian coordinate system and $\mathbf{d}_s$ is a vector that points from the reference point of the antenna array to the antenna element s. $\mathbf{f}_{UE,u,n,m}$ is also calculated using (5), but the antenna element index s has to be replaced by u and the pair of angles $(\theta_{n,m}^{ZOD}, \phi_{n,m}^{AOD})$ has to be replaced by $(\theta_{n,m}^{ZOA}, \phi_{n,m}^{AOA})$, which are the zenith angle of arrival (ZOA) and azimuth angle of arrival (AOA), respectively. In a similar manner, $\mathbf{f}_{BS,s,0}$ and $\mathbf{f}_{UE,u,0}$ are also calculated from (5), but considering the angles of arrival and departure of the single LOS component, i.e., ϕ_{LOS}^{AOA}, θ_{LOS}^{ZOA}, ϕ_{LOS}^{AOD}, and θ_{LOS}^{ZOD}.

The losses due to the cross polarization power ratio (XPR) in (4), is modeled by a 2×2 matrix $\mathbf{X}$ that combines the antenna responses of the BS and UE for each ray. The XPR matrix $\mathbf{X}$ is given by [12]:

$$
\mathbf{X} = \begin{cases} \overbrace{\begin{bmatrix} 1 & 0 \\ 0 & -1 \end{bmatrix} \exp\left(-2\pi j \frac{\|\mathbf{c}_{BS}-\mathbf{c}_{UE}\|}{\lambda}\right)}^{\mathbf{X}_0}, & \text{LOS ray,} \\[2em] \underbrace{\begin{bmatrix} \exp(j\Omega_{n,m}^{VV}) & \frac{\exp(j\Omega_{n,m}^{VH})}{\sqrt{\kappa_{n,m}}} \\ \frac{\exp(j\Omega_{n,m}^{HV})}{\sqrt{\kappa_{n,m}}} & \exp(j\Omega_{n,m}^{HH}) \end{bmatrix}}_{\mathbf{X}_{n,m}}, & \text{otherwise,} \end{cases} \quad (6)
$$

where $\mathbf{c}_{BS}$ and $\mathbf{c}_{UE}$ denote the coordinates of the BS and UE in the three dimensional (3D) space, respectively. $\Omega_{n,m}^{VV}$, $\Omega_{n,m}^{VH}$, $\Omega_{n,m}^{HV}$, and $\Omega_{n,m}^{HH}$ denote random phases generated as an independent and identically distributed (i.i.d.) uniform random variable in the range $(-\pi, \pi]$ for each ray m within the cluster n. $\kappa_{n,m}$ denotes the XPR component that quantifies the polarization changes of the transmited field throughout the propagation path. $\kappa_{n,m}$ is generated independently for each ray as a log-normal random variable, i.e., $\kappa_{n,m} = 10^{\mu_{XPR}+\sigma_{XPR}z_{n,m}}$, where μ_{XPR} and σ_{XPR} denote the mean and standard deviation of the XPR, respectively, and $z_{n,m} \sim \mathcal{N}(0, 1)$. Note that the XPR matrix $\mathbf{X}_0$ in (6) only introduces a random phase shift in the single LOS component based on the distance between the BS and the UE and does not contribute with any loss since the direct LOS path does not suffer reflections or diffractions.

Still in (4), $d_{UE,0}(t)$ and $d_{UE,n,m}(t)$ denote the complex Doppler shift experienced by the UE at time t from the single LOS component and the ray m within the cluster n, respectively. The term $d_{UE,n,m}(t)$ is given by

$$
d_{UE,n,m}(t) = \exp\left(\frac{2\pi j t}{\lambda} \mathbf{r}^T(\theta_{n,m}^{ZOA}, \phi_{n,m}^{AOA}) \mathbf{v}_{UE} \right), \quad (7)
$$

where $\mathbf{v}_{UE}$ denotes the UE velocity in the 3D space. Note that $d_{UE,0}(t)$ is also obtained from (7), but replacing the multipath wavefrom $\mathbf{r}(\theta_{n,m}^{ZOA}, \phi_{n,m}^{AOA})$ by the LOS wavefront, i.e., $\mathbf{r}(\theta_{LOS}^{ZOA}, \phi_{LOS}^{AOA})$.

C. CHANNEL GENERATION PROCEDURE

In order to generate the angles and delays for both clusters and rays in the channel model in (4), a scaled version of the CDL-A and CDL-D models of [12] (Section 7.7, tables 7.7.1-1 and 7.7.1-4) were used due to their low complexity and easy implementation. CDL models are useful for fast link and system level simulations since they consider that the channel impulse response (CIR) stays wide-sense stationary (WSS) during the simulation and there is no significant change in the angles or delays of each cluster, i.e., the CDL models consider that the scenario is almost static and the fluctuation in the CIR is due to the Doppler shift produced by the UE movement. Therefore, the use of CDL models for channel modeling in remote rural areas is well justified since the scattering objects (clusters) are mostly mountains that are located far from the receiver (transmitter), which produces small delay and angular variations.

The CDL models from [12] are tables containing the powers, the delays, and the angles of arrival and departure for both azimuth and zenith of each cluster for a generic scenario and require to be scaled to produce the delay and angular spreads for a desired scenario. For the proposed channel model, the delay and angular spreads in table 3 were considered to rescale the CDL models.

TABLE 3. Delay and angular spreads for remote areas proposed by Telstra and Ericcson [27].

DS (ns)	ASD (°)	ASA (°)	ZSD (°)	ZSA (°)
100	1	30	0.10	1

ASD: azimuth spread of departure, ASA: azimuth spread of arrival, ZSD: zenith spread of departure, ZSA: zenith spread of arrival.

In this context, the DS of both CDL models of [12] can be calculated as [16]:

$$\sigma_{\tau,\text{cdl}} = \sqrt{\sum_{n=1}^{N} P_{n,\text{cdl}}\tau_{n,\text{cdl}}^2 - \left(\sum_{n=1}^{N} P_{n,\text{cdl}}\tau_{n,\text{cdl}}\right)^2}, \quad (8)$$

where $\tau_{n,\text{cdl}}$ and $P_{n,\text{cdl}}$, $n = 1, \ldots, N$, denote the delays and normalized cluster powers from the CDL models. Using (8), the delays of each cluster of the proposed model are obtained as follows:

$$\tau_n = \frac{\sigma_\tau}{\sigma_{\tau,\text{cdl}}}\tau_{n,\text{cdl}}, \quad n = 1, \ldots, N, \quad (9)$$

where σ_τ is the desired DS given in table 3. To scale the AOAs, a similar procedure as the one described above is used, i.e., first it is computed the azimuth spread of arrival (ASA) for both CDL models, as follows:

$$\sigma_{\text{ASA,cdl}} = \sqrt{\sum_{n=1}^{N} P_{n,\text{cdl}}\left(\phi_{n,\text{cdl}}^{\text{AOA}}\right)^2 - \left(\sum_{n=1}^{N} P_{n,\text{cdl}}\phi_{n,\text{cdl}}^{\text{AOA}}\right)^2}, \quad (10)$$

where $\phi_{n,\text{cdl}}^{\text{AOA}}$, $n = 1, \ldots, N$, denote the AOAs from CDL models. Next, it is used (10) to obtain the scaled AOAs, as follows:

$$\phi_n^{\text{AOA}} = \frac{\sigma_{\text{ASA}}}{\sigma_{\text{ASA,cdl}}}\phi_{n,\text{cdl}}^{\text{AOA}}, \quad n = 1, \ldots, N, \quad (11)$$

where σ_{ASA} is the desired ASA from table 3. Note that, to scale the AODs, ZOAs and, ZODs for each cluster in the proposed model, it is also used the equations (10) and (11) along with the correspondent angles substitution. Finally, table 4 shows some of the values for the delays and angles of the proposed channel model which were obtained by the procedure described above.

Now, using the scaled angles and delays in table 4, the procedure to generate the CIR in (4) is described in six steps, as follows:

1) Define the Cartesian and spherical coordinate systems and the transformation between them as follows [12]: let $\mathbf{r} = \begin{bmatrix} x & y & z \end{bmatrix}^{\text{T}}$ be a vector in Cartesian coordinate system and a pair of angles (ϕ, θ), $\phi \in (-180°, 180°]$ and $\theta \in [0°, 180°]$, in spherical coordinate system, then the transformation between $\mathbf{r}$ and (ϕ, θ) is related as:

$$\mathbf{r} = \|\mathbf{r}\| \begin{bmatrix} \cos(\phi)\sin(\theta) & \sin(\phi)\sin(\theta) & \cos(\theta) \end{bmatrix}^{\text{T}}, \quad (12)$$

$$\phi(\mathbf{r}) = \tan^{-1}\left(\begin{bmatrix} 0 & 1 & 0 \end{bmatrix}\frac{\mathbf{r}}{\|\mathbf{r}\|}, \begin{bmatrix} 1 & 0 & 0 \end{bmatrix}\frac{\mathbf{r}}{\|\mathbf{r}\|}\right), \quad (13)$$

$$\theta(\mathbf{r}) = \cos^{-1}\left(\begin{bmatrix} 0 & 0 & 1 \end{bmatrix}\frac{\mathbf{r}}{\|\mathbf{r}\|}\right), \quad (14)$$

respectively. Note that $\tan^{-1}(\cdot, \cdot)$ and $\cos^{-1}(\cdot)$ in (13) and (14), respectively, denote the arctangent function (which takes into account the sign of its input arguments) and the arccosine function.

2) Set the network layout, i.e., the BS and UEs locations, the parameters of the antenna arrays in (5) (e.g., radiation power pattern Ψ, system frequency and polarization angle ξ) and compute the angles of the LOS component using (12)-(14), as follows:

$$\phi_{\text{LOS}}^{\text{AOD}} = \phi\left(\mathbf{c}_{\text{BS}} - \mathbf{c}_{\text{UE}}\right), \quad \theta_{\text{LOS}}^{\text{ZOD}} = \theta\left(\mathbf{c}_{\text{BS}} - \mathbf{c}_{\text{UE}}\right), \quad (15)$$

$$\phi_{\text{LOS}}^{\text{AOA}} = \phi\left(\mathbf{c}_{\text{UE}} - \mathbf{c}_{\text{BS}}\right), \quad \theta_{\text{LOS}}^{\text{ZOA}} = \theta\left(\mathbf{c}_{\text{UE}} - \mathbf{c}_{\text{BS}}\right). \quad (16)$$

3) Using (9), (11), (15) and (16), it is determined the power, delays and angles for each ray within each cluster as follows [12]:

$$P_{n,m} = P_{n,\text{cdl}}/M, \forall(n, m), \quad (17)$$

$$\tau_{n,m} = \tau_n, \forall(n, m), \quad (18)$$

$$\phi_{n,m}^{\text{AOD}} = \phi_n^{\text{AOD}} + \phi_{\text{LOS}}^{\text{AOD}} + c_{\text{ASD}}\,\alpha_m, \forall(n, m), \quad (19)$$

$$\phi_{n,m}^{\text{AOA}} = \phi_n^{\text{AOA}} + \phi_{\text{LOS}}^{\text{AOA}} + c_{\text{ASA}}\,\alpha_m, \forall(n, m), \quad (20)$$

$$\theta_{n,m}^{\text{ZOD}} = \theta_n^{\text{ZOD}} + \theta_{\text{LOS}}^{\text{ZOD}} + c_{\text{ZSD}}\,\alpha_m, \forall(n, m), \quad (21)$$

$$\theta_{n,m}^{\text{ZOA}} = \theta_n^{\text{ZOA}} + \theta_{\text{LOS}}^{\text{ZOA}} + c_{\text{ZSA}}\,\alpha_m, \forall(n, m), \quad (22)$$

where $P_{n,m}$ and $\tau_{n,m}$ denote the power and delay of the ray m within the cluster n, respectively. Moreover, $c_{\text{ASD}}, c_{\text{ASA}}, c_{\text{ZSD}}$ and c_{ZSA} are the specif per-cluster angular spread defined in table 6 and α_m is the specif ray offset defined in table 5.

4) Generate the initial phases and the XPR in (6) independently for each ray as follows: the initial phases are uniformly distributed in the range $(-180°, 180°]$ and the XPR $\kappa_{n,m}$ is given by [12]:

$$\kappa_{n,m} = 10^\chi, \quad (23)$$

where χ follows a Normal distribution with mean and standard deviation given by $\mu_{\text{XPR}} = 7\,\text{dB}$ and $\sigma_{\text{XPR}} = 3\,\text{dB}$ [12], respectively.

5) Compute the path loss and shadow fading using the parameters from table 2.

6) Finally, the channel coefficients are generated in (4) by combining the path loss, SF and the scaled CDL profile from (17)-(23) for each pair of antenna elements (u, s).

TABLE 4. Scaled angle and delays of the proposed channel model.

(a) CDL-A model.

Cluster	Delay (ns)	AOD (°)	AOA (°)	ZOD (°)	ZOA (°)
1	0	-2.422	15.482	0.177	6.009
2	38.19	-0.057	-46.083	0.328	4.375
3	40.25	-0.057	-46.083	0.328	4.375
⋮	⋮	⋮	⋮	⋮	⋮
21	500.66	-2.096	-30.782	0.605	6.996
22	530.43	1.720	-45.811	0.080	7.221
23	965.86	-0.764	16.659	0.510	7.480

(b) CDL-D model.

Cluster	Delay (ns)	AOD (°)	AOA (°)	ZOD (°)	ZOA (°)
1 (LOS ray)	0	0	-72.816	4.408	69.946
2	0	0	-72.816	4.408	69.946
3	3.5	5.714	36.084	3.827	74.580
⋮	⋮	⋮	⋮	⋮	⋮
12	942.4	3.369	-48.382	4.646	74.666
13	970.8	-8.462	-3.681	3.594	60.591
14	1252.5	4.945	-33.900	3.871	62.565

TABLE 5. Offset for each ray within a cluster [12].

Ray index m	1, 2	3, 4	5, 6	7, 8	9, 10	11, 12	13, 14	15, 16	17, 18	19, 20
Offset α_m	±0.0447	±0.1413	±0.2492	±0.3715	±0.5129	±0.6797	±0.8844	±1.1481	±1.5195	±2.1551

IV. SIMULATION RESULTS

This section presents analytical and numerical simulations exploiting different characteristics of the proposed channel model for rural remote areas. First, aiming to validate the model, its ACF was computed numerically and analytically, showing a good agreement between both results. Next, numerical simulations were performed for the MIMO case, using the EVD to analyze the suitability of the channel to provide spatial multiplexing and/or beamforming. Finally, an analysis of the achievable data rate considering the proposed channel model is done for different MIMO configurations with SP and DP antennas to identify the best configuration to achieve the target key performance indicator (KPI) of the 5G-RANGE project, i.e., to deliver 100 Mbps for a single UE at the cell-edge.

TABLE 6. Per-cluster angular spreads [12].

c_{ASD} (°)	c_{ASA} (°)	c_{ZSD} (°)	c_{ZSA} (°)
5	8	3	3

Table 7 contains the main parameters used to perform the simulations in this paper.

A. CHANNEL METRICS EVALUATION

Assuming a vertically-polarized antenna at both the transmitter (Tx) and the receiver (Rx), a closed-form expression for the ACF of the proposed channel model for both CDL-A and CDL-D are derived (see Appendix), which gives:

$$
R(n_\lambda, F) = \frac{\mathrm{E}\left[H_{1,1}(t,f)H_{1,1}^*(t+T, f+F)\right]}{\sqrt{\mathrm{E}\left[|H_{1,1}(t,f)|^2\right]\mathrm{E}\left[|H_{1,1}(t+T, f+F)|^2\right]}}
$$

$$
= \sum_{n=1}^{N}\sum_{m=1}^{M}\frac{P_n}{1+K_\mathrm{R}}J_0\left(2\pi n_\lambda \sin(\theta_{n,m}^{ZOA})\right)\exp(j2\pi\tau_n F)
$$

$$
+ \frac{K_\mathrm{R}}{1+K_\mathrm{R}}J_0\left(2\pi n_\lambda \sin(\theta_{LOS}^{ZOA})\right), \qquad (24)
$$

where E[·] denotes the expectation operator, $H_{1,1}(\cdot)$ denotes the CIR in frequency domain obtained from the non-discrete Fourier transform (NDFT) [36], $J_0(\cdot)$ denotes the Bessel function of first kind and zero-order and, n_λ corresponds to the number of wavelengths traveled by the UE, defined as:

$$
n_\lambda = \frac{\|\mathbf{v}_{UE}\|\,T}{\lambda}, \qquad (25)
$$

where T, F and, λ denote the time shift, the frequency shift and, wavelength, respectively.

Figure 4 depicts the real and complex part of the analytical and empirical ACFs in (24) considering both CDL-A (NLOS) and CDL-D (LOS) models. As it can be seen in figures 4a, 4c and 4d, the correlation for the CDL-A model fluctuates much faster when compared with the correlation of the CDL-D model. This is due to the distribution of the power between the clusters on each CDL model, i.e., while in the CDL-A all the clusters present similar powers, in the CDL-D model the LOS ray contains $K_\mathrm{R} = 7.9$ times more power than all the clusters combined. This result indicates that in the CDL-A model the destructive and/or constructive combinations of the rays can produce large fluctuations in the power of the received signal. However, due to the LOS ray in the CDL-D model, the received power is approximately constant and suffers small changes as observed in these figures. Also, from (24) it is easy to verify that for $F = 0$ Hz, the complex part of $R(n_\lambda, F)$ is equals zero as depicted in figure 4b. Finally, it is noted that there is a good agreement between the analitycal and empirical curves in figure 4.

Besides the real and complex part of the ACF in (24), it is also of interest to analyze its magnitude which allows to obtain the coherence time and the coherence bandwidth of the proposed channel model. The coherence time T_c is defined in [37] as the largest time shift T such that the magnitude of the ACF in (24) stays above a given threshold ϵ_{T_c}, i.e., $|R(n_\lambda, F)| \geq \epsilon_{T_\mathrm{c}}$ with $F = 0$ Hz. Note that T_c can be obtained directly from figure 4a since the complex part of $R(n_\lambda, 0)$ is zero as dipicted in figure 4b. In this context,

(a) Real part of the ACF in (24) *vs.* n_λ with $F = 0$ Hz.

(b) Complex part of the ACF in (24) *vs.* n_λ with $F = 0$ Hz.

(c) Real part of the ACF in (24) *vs.* F with $n_\lambda = 0$.

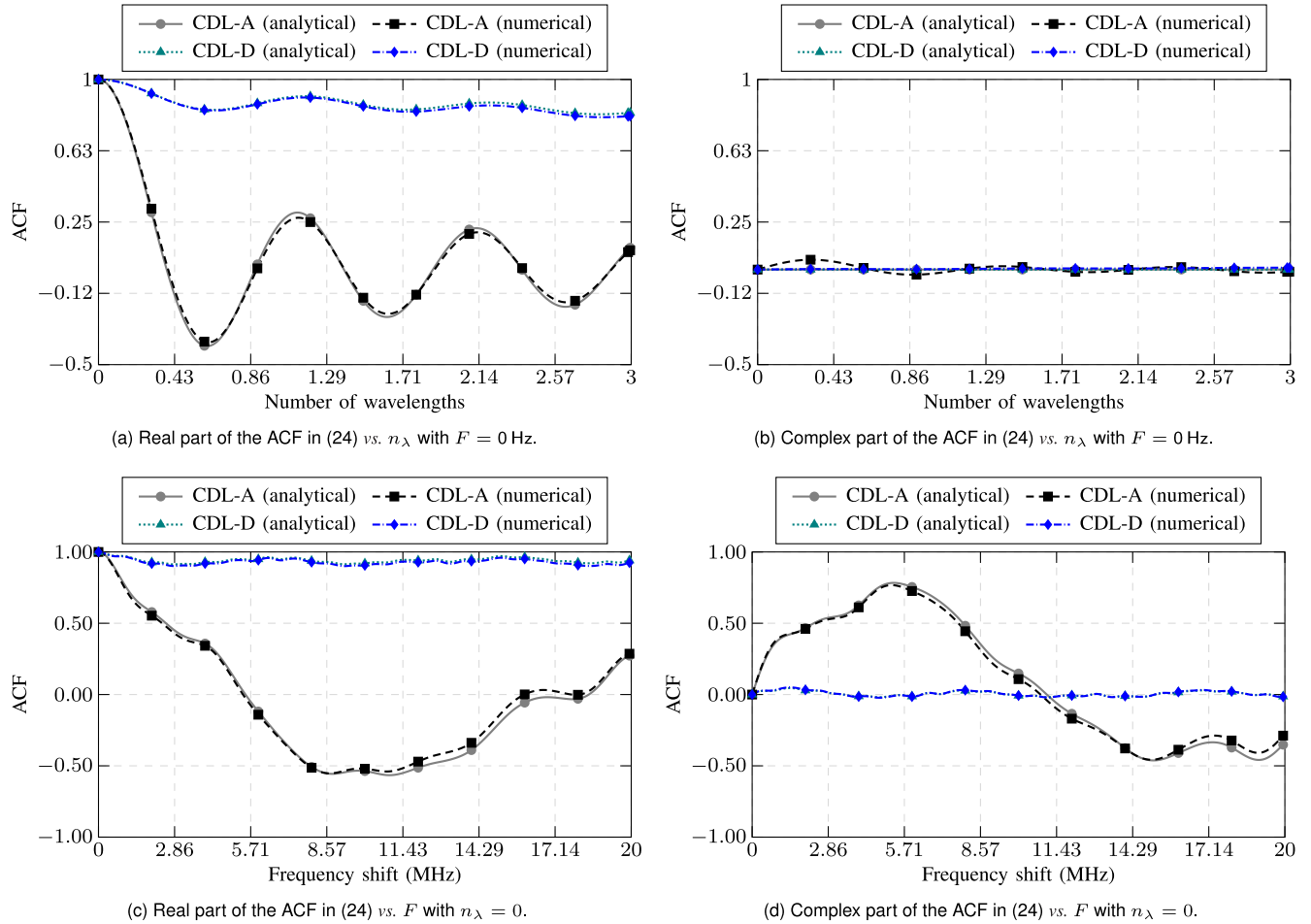(d) Complex part of the ACF in (24) *vs.* F with $n_\lambda = 0$.

FIGURE 4. Analytical and empirical ACF of the proposed channel model for both CDL-A and CDL-D.

TABLE 7. Main simulation parameters.

Parameter	Value/Info.	Unit	Ref.
Cell radius	50	km	[10]
BS transmit power	49	dBm	[10]
Eff. channel bandwidth	23.40	MHz	–
PRB bandwidth	180	kHz	[35]
Total number of PRBs	130	–	–
Carrier frequency	700	MHz	–
Path loss model	Table 2	dB	–
Shadowing std.	Table 2	dB	–
Fast fading model	Tables 4–6	–	–
Antenna config.	Up to 4×4	–	[10]
Rad. pattern (BS and UE)	Isotropic	–	–
Antenna gain (BS and UE)	9	dBi	[12]
Polarization (BS and UE)	SP and DP	°	–
Noise figure	5	dB	[10]
Noise power per PRB*	−116.45	dBm	–
Number of UEs	1	–	–
Monte Carlo runs	5000	–	–

PRB: physical resource block, UE: user equipment, BS: base station, SP: single-polarized, DP: dual-polarized.

defining $\epsilon_{T_c} = 0.9$ in figure 4a, it is obtained $n_\lambda = 0.1$ and $n_\lambda = 0.37$ for the CDL-A and CDL-D models, respectively. Finally, replacing $n_\lambda = 0.1$ and $n_\lambda = 0.37$ into (25) it provides a relation between the UE speed $\|\mathbf{v}_{UE}\|$ and the coherence time T_c for each CDL model, as depicted in fig-
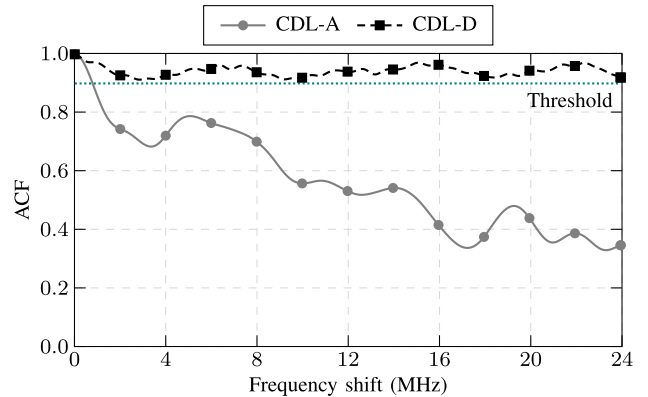

FIGURE 5. Relation between coherence time and UE speed.

ure 5. From this figure it is noted that when the UE speed increases by a factor $\eta > 0$, the coherence time T_c decays by the same factor for both CDL models. Finally, from this figure it is also possible to see that T_c for the LOS conditions is around 3.7 larger than T_c for the NLOS conditions.

Similarly to the coherence time, the coherence bandwidth B_c is defined as the largest frequency shift F such that the
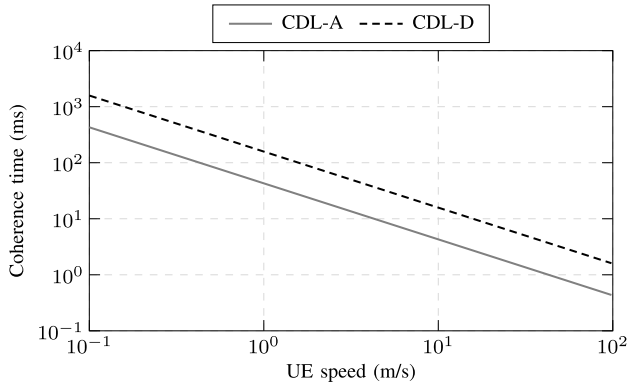
FIGURE 6. Magnitude of the ACF in (24) *vs.* the frequency shift with $n_\lambda = 0$.

magnitude of the ACF in (24) stays above a given threshold ϵ_{B_c}, i.e., $|R(n_\lambda, F)| \geq \epsilon_{B_c}$ with $n_\lambda = 0$. In this context, figure 6 shows the magnitude of the ACF in (24) versus F where it was used $\epsilon_{B_c} = 0.9$. From this figure, one can see that for the CDL-D model the correlation stays above ϵ_{B_c} for a frequency shift equals to the system bandwidth, i.e., the channel is considered as flat fading over the whole frequency range (i.e., 23.4 MHz). On the other hand, for the CDL-A model, the correlations crosses the threshold ϵ_{B_c} in $F = B_c = 0.78$ MHz which is slightly larger than the bandwidth of 4 physical resource blocks (PRBs) (see table 7).

Besides the ACF of the proposed channel model in (24), it is also of interest to analyze the number of parallel data streams that can be supported in the MIMO case. To this end, the CDF of the singular values of the proposed channel model, using equal power allocation (EPA), have been computed for a 4×4 MIMO system, as follows[2]:

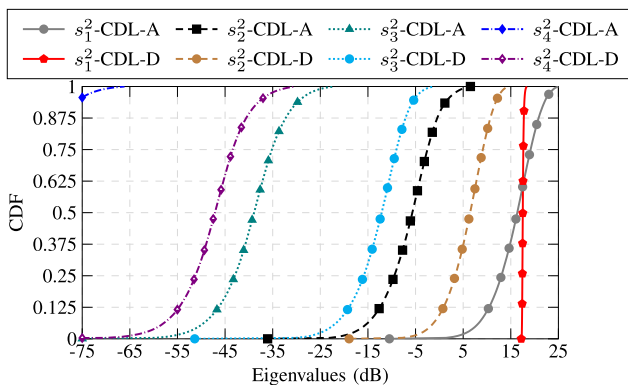**FIGURE 7.** CDF of the eigenvalues in (26) for both CDL-A and CDL-D models.

$$\mathbf{s} = \text{EVD}\left(\frac{\mathbf{H}_k \mathbf{H}_k^{\text{H}}}{10^{-0.1(\text{PL}+\text{SF})}}\right), \quad k = 1, \ldots, N_{\text{PRB}}, \quad (26)$$

[2]Note that the normalization by $10^{-0.1(\text{PL}+\text{SF})}$ in (26) is required to remove the effects of the large scale fading.

where EVD denotes the eigenvalue decomposition operation, $\mathbf{H}_k$ is the 4×4 channel matrix in frequency domain at PRB k, $(\cdot)^{\text{H}}$ denotes the complex transpose operation and, $\mathbf{s} = \left[s_1^2\ s_2^2\ s_3^2\ s_4^2\right]^{\text{T}}$ denotes a column vector composed of four eigenvalues sorted in ascending order, i.e., $s_1^2 \geq s_2^2 \geq s_3^2 \geq s_4^2$. In this context, figure 7 depicts the CDF of the eigenvalues in (26), in dB, for both CDL-A and CDL-D models. As it can be seen in this figure, for the CDL-A model, the gap between the CDF of the first and second eigenvalues is around 20 dB and becomes larger than 50 dB for the other eigenvalues. On the other hand, for the CDL-D model, note that the CDF of the first eigenvalue has a gain around 10 dB when compared with the CDF of the second eigenvalue and this gain becomes larger than 30 dB in comparision with the third and fourth eigenvalues. Moreover, note that the CDF of the first eigenvalue of the CDL-D is almost a vertical line and suffers small fluctuations. This happens because the power of the received signal is mostly composed by the single LOS component that suffers only slight variations caused by constructive/destructive combinations of the other (weaker) multipath components.

In this context, from figure 7 it is noted that the channel matrices of both CDL-A and CDL-D models are ill-conditioned, with the difference that in the CDL-D model, the LOS component concentrates most of the channel energy (first eigenvalue). A possible physical explanation for this is that, due to the small angular spread in table 3, the NLOS components present a high correlation. In other words, the number of parallel streams supported by the channel will be less than four. However, taking into account that the channel state information (CSI) is known at the transmitter side, capacity maximization techniques could be employed to improve the spatial multiplexing gain, such as the water-filling.

B. ANALYSIS OF THE ACHIEVABLE DATA RATE

To analyze the achievable data rate and also the spatial correlation of the MIMO channels, the CDF of the throughput was calculated considering SISO and MIMO (2×2 and 4×4) configurations using SP and DP antennas, without considering any coding and/or frame structure, and with the UE placed at cell-edge. That metric was computed using the Shannon formula for both SISO and MIMO channels, i.e.:

$$r = \sum_{k=1}^{N_{\text{PRB}}} B \log_2\left(\det\left[\mathbf{I} + \frac{P_{\text{BS}}\mathbf{H}_k \mathbf{H}_k^{\text{H}}}{N_{\text{PRB}} N_{\text{BS}} \gamma^2}\right]\right), \quad (27)$$

where N_{PRB} is the number of PRBs, B is the bandwidth of each PRB, $\mathbf{I}$ denotes the identity matrix of size N_{UE}, N_{BS} and N_{UE} denote the number of antenna elements at the BS and UE, respectively, P_{BS} is the BS transmitted power and γ^2 is the noise power in a PRB.

In this context, figures 8a and 8b show the throughput in (27) assuming NLOS and LOS cases, respectively, for SISO and MIMO (2×2 and 4×4) configurations considering both SP and DP antennas with the UEs placed at cell-edge. As it

(a) CDL-A channel model.
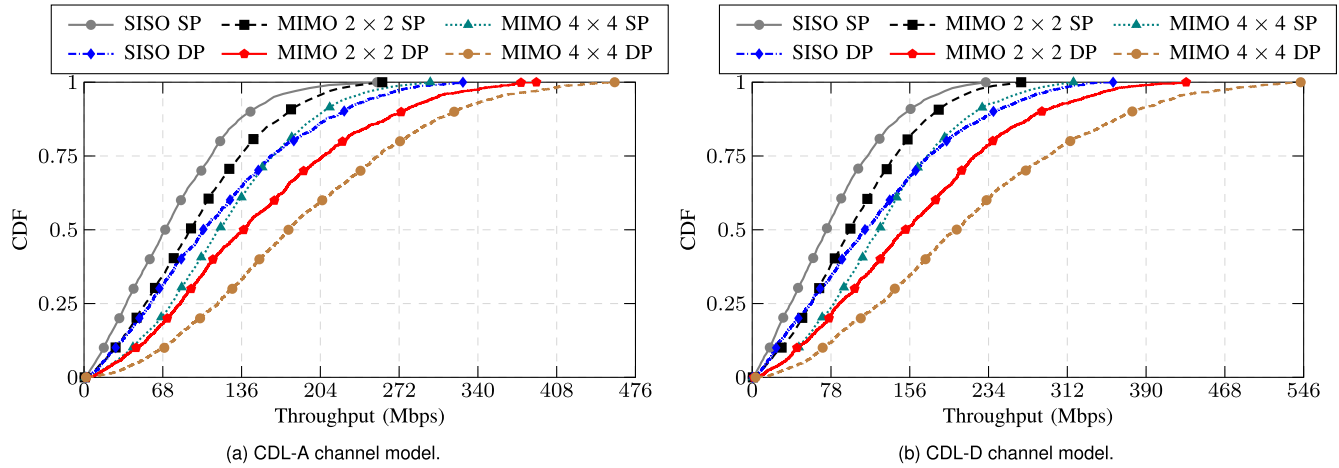
(b) CDL-D channel model.

FIGURE 8. Achievable data rate using the proposed channel model with the UE located at the cell-edge.

TABLE 8. Percentage of time in which the KPI of 100 Mbps is achieved for each scenario.

	SISO		MIMO 2 × 2		MIMO 4 × 4	
	SP	DP	SP	DP	SP	DP
CDL-A	30	50	42	66	60	80
CDL-D	31	54	47	69	64	82

SISO: single-input single-output, MIMO: multiple-input multiple-output, SP: single-polarized, DP: dual-polarized, NLOS: non-line-of-sight, LOS: line-of-sight.

can be observed in the 50th percentile of figure 8a, all DP configurations achieve at least 100 Mbps, while in the case of SP antennas, this value is only achieved for the 4×4 MIMO configuration. It can also be observed that the DP SISO configuration outperforms the SP 2×2 MIMO case. These results are in accordance with the fact that in rural and remote areas the propagation channel exhibits a poor scattering and a small angular spread, leading to a high spatial correlation between the antenna elements at both BS and UE. Therefore, the benefits of polarization diversity becomes more effective than the array gain [29]. Now, analyzing the 50th percentile of figure 8b, it is noted that the throughput of DP SISO configuration is approximately the same as the SP 4×4 MIMO, and even supersedes it for higher percentiles, indicating that the virtualization of the array using DP antennas (thus creating parallel subchannels paths) is preferable than physically increasing the array size by using more antenna elements. It is worth mentioning that, the simulations presented in figure 8 are upper-bound curves since they were generated from the Shannon's capacity formula.

Finally, to obtain a better understanding of the impact of the results of figures 8a and 8b, table 8 shows the percentage of time where the system achieves the KPI of 100 Mbps. An interesting result that can be easily extracted from this table is that all the BS-UE transmissions using DP antennas achieve the KPI at least on average, i.e., 50 % of the time.

V. CONCLUSION

In this paper, a CDL-based channel model was developed for 5G MIMO systems (up to 4×4) for remote rural areas with a maximum distance of 50 km. The model was derived by combining the measured data from [11] with the CDL-A and CDL-D profiles from [12]. The model is simple to implement and useful to perform fast link-level and system-level simulations.

To validate the proposed channel model, its ACF was derived analitycally and compared with a numerical simulation showing a good agreement between both results. Furthermore, numerical simulations have shown that the proposed model has the potential to transmit one and two data streams for the CDL-A and CDL-D profiles, respectively. Also, the system achievable data rate at the cell-edge was evaluated for SISO and MIMO configurations (2×2 and 4×4) considering SP and DP antennas. The results indicate that the DP SISO outperforms the SP 2×2 MIMO and also the DP 2×2 MIMO outperforms the SP 4×4 MIMO. These results corroborate the use of DP arrays in MIMO systems operating in rural and remote areas, which is particularly attractive in VHF and UHF bands, where the size of the array is large.

Therefore, the study performed in this paper can be used as a first insight of what can be achieved in a remote rural area in terms of throughput and spatial multiplexing. However, the model still can be refined by performing a detailed study involving field trials in a larger set of remote areas.

APPENDIX

Considering a single antenna element vertically polarized in both Tx and Rx, the general form for the CIR in (4) can be expressed as:

$$h_{1,1}(t, \tau)$$

$$= \sum_{n=1}^{N} \sum_{m=1}^{M} \sqrt{p_n} \exp\left(\frac{2\pi jt}{\lambda} \mathbf{r}^{\mathrm{T}}(\theta_{n,m}^{\mathrm{ZOA}}, \phi_{n,m}^{\mathrm{AOA}}) \mathbf{v}_{\mathrm{UE}} \right)$$

$$\times \exp\left(j\Omega_{n,m}^{VV}\right)\delta(\tau-\tau_n)+\exp\left(\frac{2\pi jt}{\lambda}\mathbf{r}^T(\theta_{LOS}^{ZOA},\phi_{LOS}^{AOA})\mathbf{v}_{UE}\right)$$
$$\times\sqrt{p_{LOS}}\exp(j\Omega_{LOS})\,\delta(\tau-\tau_0), \tag{28}$$

where $p_n = P_n/[M(1+K_R)]$, $p_{LOS} = K_R/(1+K_R)$ and, $\Omega_{LOS} = -2\pi\,\|\mathbf{c}_{BS}-\mathbf{c}_{UE}\|\,/\lambda$ is the initial phase of the LOS ray obtained from (6). Assuming that the mobility of the UE is in the horizontal plane, the inner product $\mathbf{r}^T(\theta,\phi)\mathbf{v}_{UE}$ in (28), with $(\theta,\phi)\in\{(\theta_{n,m}^{ZOA},\phi_{n,m}^{AOA}),(\theta_{LOS}^{ZOA},\phi_{LOS}^{AOA})\}$, can be rewritten as:

$$\mathbf{r}^T(\theta,\phi)\mathbf{v}_{UE}$$
$$= \|\mathbf{v}_{UE}\|\begin{bmatrix}\cos(\beta) & \sin(\beta) & 0\end{bmatrix}\begin{bmatrix}\cos(\phi)\sin(\theta)\\\sin(\phi)\sin(\theta)\\\cos(\theta)\end{bmatrix}$$
$$= \|\mathbf{v}_{UE}\|\sin(\theta)\cos(\phi-\beta), \tag{29}$$

where β denotes the direction of the UE velocity in the horizontal plane. Replacing (29) into (28) yields:

$$h_{1,1}(t,\tau)$$
$$= \sum_{n=1}^{N}\sum_{m=1}^{M}\sqrt{p_n}\exp\left(jt\overbrace{\frac{2\pi}{\lambda}\|\mathbf{v}_{UE}\|\sin(\theta_{n,m}^{ZOA})\cos(\phi_{n,m}^{AOA}-\beta)}^{v_{n,m}(\beta)}\right)$$
$$\times\exp\left(j\Omega_{n,m}^{VV}\right)\delta(\tau-\tau_n)+\sqrt{p_{LOS}}\exp(j\Omega_{LOS})\,\delta(\tau-\tau_0)$$

$$\times\exp\left(jt\underbrace{\frac{2\pi}{\lambda}\|\mathbf{v}_{UE}\|\sin(\theta_{LOS}^{ZOA})\cos(\phi_{LOS}^{AOA}-\beta)}_{v_{LOS}(\beta)}\right). \tag{30}$$

Next, applying the Fourier transform in (30) yields:

$$H_{1,1}(t,f)$$
$$=\int_{-\infty}^{\infty}h_{1,1}(t,\tau)\exp(-j2\pi\tau f)d\tau=\sum_{n=1}^{N}\sum_{m=1}^{M}\sqrt{p_n}$$
$$\times\exp\left(jtv_{n,m}(\beta)\right)\exp\left(j\Omega_{n,m}^{VV}\right)\exp(-j2\pi\tau_n f)$$
$$+\sqrt{p_{LOS}}\exp\left(jtv_{LOS}(\beta)\right)\exp(j\Omega_{LOS})\exp\left(-j2\pi\tau_0 f\right), \tag{31}$$

and its corresponding ACF $R(t,T,f,F)$ is given by:

$$R(t,T,f,F)=\frac{E\left[H_{1,1}(t,f)H_{1,1}^{*}(t+T,f+F)\right]}{\sqrt{E\left[|H_{1,1}(t,f)|^2\right]E\left[|H_{1,1}(t+T,f+F)|^2\right]}}$$
$$= E\left[H_{1,1}(t,f)H_{1,1}^{*}(t+T,f+F)\right], \tag{32}$$

where

$$E\left[|H_{1,1}(t,f)|^2\right]=E\left[|H_{1,1}(t+T,f+F)|^2\right]=\sum_{n=1}^{N}P_n=1.$$

Next, replacing (31) into (32) allows to expand $R(t,T,f,F)$ which is given by (33), as shown at the bottom of the page.

$$R(t,T,f,F)$$
$$= E\Bigg\{\Bigg[\sum_{n=1}^{N}\sum_{m=1}^{M}\sqrt{p_n}\exp\left(jtv_{n,m}(\beta)\right)\exp\left(j\Omega_{n,m}^{VV}\right)\exp(-j2\pi\tau_n f)+\sqrt{p_{LOS}}\exp\left(jtv_{LOS}(\beta)\right)\exp(j\Omega_{LOS})$$
$$\times\exp\left(-j2\pi\tau_0 f\right)\Bigg]\Bigg[\sum_{x=1}^{N}\sum_{y=1}^{M}\sqrt{p_x}\exp\left(-jtv_{x,y}(\beta)\right)\exp\left(-jTv_{x,y}(\beta)\right)\exp\left(-j\Omega_{x,y}^{VV}\right)\exp(j2\pi\tau_x f)\exp(j2\pi\tau_x F)$$
$$+\sqrt{p_{LOS}}\exp\left(-jtv_{LOS}(\beta)\right)\exp\left(-jTv_{LOS}(\beta)\right)\exp\left(-j\Omega_{LOS}\right)\exp\left(j2\pi\tau_0 f\right)\exp\left(j2\pi\tau_0 F\right)\Bigg]\Bigg\}$$

$$=\overbrace{\sum_{n=1}^{N}\sum_{m=1}^{M}\sum_{x=1}^{N}\sum_{y=1}^{M}E\{\sqrt{p_n p_x}\exp\left[jt(v_{n,m}(\beta)-v_{x,y}(\beta))\right]\exp\left[j(\Omega_{n,m}^{VV}-\Omega_{x,y}^{VV})\right]\exp\left[j2\pi f(\tau_x-\tau_n)\right]\exp\left(-jTv_{x,y}(\beta)\right)\exp(j2\pi\tau_x F)\}}^{A}$$

$$+\overbrace{\sum_{n=1}^{N}\sum_{m=1}^{M}E\{\sqrt{p_n p_{LOS}}\exp\left[jt(v_{n,m}(\beta)-v_{LOS}(\beta))\right]\exp\left[j(\Omega_{n,m}^{VV}-\Omega_{LOS})\right]\exp\left[j2\pi f(\tau_0-\tau_n)\right]\exp\left(-jTv_{LOS}(\beta)\right)\exp(j2\pi\tau_0 F)\}}^{B}$$

$$+\overbrace{\sum_{x=1}^{N}\sum_{y=1}^{M}E\{\sqrt{p_x p_{LOS}}\exp\left[jt(v_{LOS}(\beta)-v_{x,y}(\beta))\right]\exp\left[j(\Omega_{LOS}-\Omega_{x,y}^{VV})\right]\exp\left[j2\pi f(\tau_x-\tau_0)\right]\exp\left(-jTv_{x,y}(\beta)\right)\exp(j2\pi\tau_x F)\}}^{C}$$

$$+\overbrace{E\{p_{LOS}\exp\left(-jTv_{LOS}(\beta)\right)\exp\left(j2\pi\tau_0 F\right)\}}^{D}. \tag{33}$$

Due to the static characteristics of the CDL model, the only random variables in the terms A, B, C and, D in (33) are the initial random phases $\Omega_{n,m}^{VV}, \forall(n, m)$, and the direction of the UE velocity especified by the angle β. Besides that, it is assumed that β and $\Omega_{n,m}^{VV}$ are independent. Under this assumptions, A, B and, C can be reorganized, respectively, as follows:

$$
A = \sum_{\substack{n=1 \\ m=1}}^{N,M} \sum_{\substack{x=1 \\ y=1}}^{N,M} \sqrt{p_n p_x}\, \mathrm{E}\big\{ \exp\big[jt(\nu_{n,m}(\beta)-\nu_{x,y}(\beta))\big]
$$

$$
\times \exp\big(-jT\nu_{x,y}(\beta)\big)\big\} \overbrace{\mathrm{E}\big\{ \exp\big[j(\Omega_{n,m}^{VV}-\Omega_{x,y}^{VV})\big]\big\}}^{A'}
$$

$$
\times \exp[j2\pi f(\tau_x-\tau_n)]\exp(j2\pi\tau_x F), \qquad (34)
$$

$$
B = \sum_{n=1}^{N} \sum_{m=1}^{M} \sqrt{p_n p_{LOS}}\, \mathrm{E}\big\{ \exp\big[jt(\nu_{n,m}(\beta)-\nu_{LOS}(\beta))\big]
$$

$$
\times \exp\big(-jT\nu_{LOS}(\beta)\big)\big\} \overbrace{\mathrm{E}\big\{ \exp\big[j(\Omega_{n,m}^{VV}-\Omega_{LOS})\big]\big\}}^{B'}
$$

$$
\times \exp[j2\pi f(\tau_0-\tau_n)]\exp(j2\pi\tau_0 F), \qquad (35)
$$

$$
C = \sum_{x=1}^{N} \sum_{y=1}^{M} \sqrt{p_x p_{LOS}}\, \mathrm{E}\big\{ \exp\big[jt(\nu_{LOS}(\beta)-\nu_{x,y}(\beta))\big]\times
$$

$$
\exp\big(-jT\nu_{x,y}(\beta)\big)\big\} \overbrace{\mathrm{E}\big\{ \exp\big[j(\Omega_{LOS}-\Omega_{x,y}^{VV})\big]\big\}}^{C'}
$$

$$
\times \exp[j2\pi f(\tau_x-\tau_0)]\exp(j2\pi\tau_x F). \qquad (36)
$$

Since the initial phases are independent and identically distributed uniform random variables, the terms A', B' and, C' in (34)-(36) are given by:

$$
A' = \begin{cases} 1, & \text{if } n = x \text{ and } m = y, \\ 0, & \text{otherwise.} \end{cases} \qquad (37)
$$

$$
B' = 0 \quad \text{and} \quad C' = 0. \qquad (38)
$$

From (38) it is noted that $B = C = 0$ and using (37) allows to rewrite A as follows:

$$
A = \sum_{n=1}^{N} \sum_{m=1}^{M} p_n \overbrace{\mathrm{E}\big\{ \exp\big(-jT\nu_{n,m}(\beta)\big)\big\}}^{A''} \exp(j2\pi\tau_n F), \quad (39)
$$

and recalling that $\nu_{n,m}(\beta) = \frac{2\pi}{\lambda} \|\mathbf{v}_{UE}\| \sin(\theta_{n,m}^{ZOA})\cos(\phi_{n,m}^{AOA}-\beta)$, A'' in (39) is simplified to:

$$
A'' = \mathrm{E}\left\{ \cos\left[T\frac{2\pi}{\lambda} \|\mathbf{v}_{UE}\| \sin(\theta_{n,m}^{ZOA})\cos(\phi_{n,m}^{AOA}-\beta)\right]\right\}
$$

$$
-j\mathrm{E}\left\{ \sin\left[T\frac{2\pi}{\lambda} \|\mathbf{v}_{UE}\| \sin(\theta_{n,m}^{ZOA})\cos(\phi_{n,m}^{AOA}-\beta)\right]\right\}
$$

$$
= \underbrace{\mathrm{E}\left\{ \cos\left[T\frac{2\pi}{\lambda} \|\mathbf{v}_{UE}\| \sin(\theta_{n,m}^{ZOA})\cos(\beta)\right]\right\}}_{J_0\left(2\pi \frac{\|\mathbf{v}_{UE}\|T}{\lambda} \sin(\theta_{n,m}^{ZOA})\right)}
$$

$$
\underbrace{-j\mathrm{E}\left\{ \sin\left[T\frac{2\pi}{\lambda} \|\mathbf{v}_{UE}\| \sin(\theta_{n,m}^{ZOA})\cos(\beta)\right]\right\}}_{=0}. \qquad (40)
$$

where $J_0(\cdot)$ is the Bessel function of first kind and zero-order. Finally, replacing (40) into (39), yields a compact form for A as function of the known channel parameters, i.e.:

$$
A = \sum_{n=1}^{N} \sum_{m=1}^{M} p_n J_0\left(2\pi \frac{\|\mathbf{v}_{UE}\| T}{\lambda} \sin(\theta_{n,m}^{ZOA})\right) \exp(j2\pi\tau_n F). \qquad (41)
$$

Note that the result from (40) can also be used to simplify the term D in (33), i.e.:

$$
D = p_{LOS}J_0\left(2\pi \frac{\|\mathbf{v}_{UE}\| T}{\lambda} \sin(\theta_{LOS}^{ZOA})\right), \qquad (42)
$$

where it was assumed $\tau_0 = 0$ s. Therefore, recalling that $B = C = 0$ and the terms A and D are given by (41) and (42), respectively, a closed for expression for $R(t, T, f, F)$ in (33) is obtained as follows:

$$
R(t, T, f, F)
$$
$$
= \frac{K_R}{1+K_R}J_0\left(2\pi \frac{\|\mathbf{v}_{UE}\| T}{\lambda} \sin(\theta_{LOS}^{ZOA})\right)
$$
$$
+ \sum_{n=1}^{N}\sum_{m=1}^{M} \frac{P_n}{1+K_R}J_0\left(2\pi \frac{\|\mathbf{v}_{UE}\| T}{\lambda} \sin(\theta_{n,m}^{ZOA})\right)\exp(j2\pi\tau_n F),
$$

which can be simplified to $R(n_\lambda, F)$:

$$
R(n_\lambda, F)
$$
$$
= \frac{K_R}{1+K_R}J_0\left(2\pi n_\lambda \sin(\theta_{LOS}^{ZOA})\right)
$$
$$
+ \sum_{n=1}^{N} \sum_{m=1}^{M} \frac{P_n}{1+K_R}J_0\left(2\pi n_\lambda \sin(\theta_{n,m}^{ZOA})\right) \exp(j2\pi\tau_n F), \qquad (43)
$$

where n_λ denotes the number of wavelengths traveled by the UE, defined as:

$$
n_\lambda = \frac{\|\mathbf{v}_{UE}\| T}{\lambda}. \qquad (44)
$$

Note that the proposed channel model is a WSS process since its ACF in (43) only depends on T (or n_λ) and F.

REFERENCES

[1] Making 5G a Reality: Addressing the Strong Mobile Broadband Demand in 2019 & Beyond, Qualcomm, Nokia, Espoo, Finland, Sep. 2017.

[2] Minimum Requirements Related to Technical Performance for IMT-2020 Radio Interface(s), document ITU-R M.2410-0, Nov. 2017.

[3] C. F. M. e Silva and F. R. P. Cavalcanti, "Techno-economic evaluation for TV white spaces," in TV White Space Communications and Networks (Woodhead Publishing Series in Electronic and Optical Materials), R. Stewart, D. Crawford, and A. Stirling, Eds., 1st ed. Oxford, U.K.: Woodhead Publishing, 2018, pp. 151–191, doi: 10.1016/B978-0-08-100611-5.00011-4.

[4] L. Chiaraviglio, N. Blefari-Melazzi, W. Liu, J. A. Gutierrez, J. Van De Beek, R. Birke, L. Chen, F. Idzikowski, D. Kilper, J. P. Monti, and J. Wu, "5G in rural and low-income areas: Are we ready?" in Proc. ITU Kaleidoscope, ICTs Sustain. World, Nov. 2016, pp. 1–8.

[5] S. Nandi, S. Thota, A. Nag, S. Divyasukhananda, P. Goswami, A. Aravindakshan, R. Rodriguez, and B. Mukherjee, "Computing for rural empowerment: Enabled by last-mile telecommunications," *IEEE Commun. Mag.*, vol. 54, no. 6, pp. 102–109, Jun. 2016.

[6] P. Rost, C. J. Bernardos, A. De Domenico, M. Di Girolamo, M. Lalam, A. Maeder, D. Sabella, and D. Wübben, "Cloud technologies for flexible 5G radio access networks," *IEEE Commun. Mag.*, vol. 52, no. 5, pp. 68–76, May 2014.

[7] P. Demestichas, A. Georgakopoulos, D. Karvounas, K. Tsagkaris, V. Stavroulaki, J. Lu, C. Xiong, and J. Yao, "5G on the horizon: Key challenges for the radio-access network," *IEEE Veh. Technol. Mag.*, vol. 8, no. 3, pp. 47–53, Sep. 2013.

[8] D. Gurney, G. Buchwald, L. Ecklund, S. L. Kuffner, and J. Grosspietsch, "Geo-location database techniques for incumbent protection in the TV white space," in *Proc. 3rd IEEE Symp. New Frontiers Dyn. Spectr. Access Netw.*, Oct. 2008, pp. 1–9.

[9] H. Bogucka, M. Parzy, P. Marques, J. W. Mwangoka, and T. Forde, "Secondary spectrum trading in TV white spaces," *IEEE Commun. Mag.*, vol. 50, no. 11, pp. 121–129, Nov. 2012.

[10] 5G-RANGE, "Application and requirements report," Remote area Access Network for the 5th GEneration (5G-RANGE), Deliverable 2.1, Apr. 2018. Accessed: Sep. 2020. [Online]. Available: http://5g-range.eu/wp-content/uploads/2018/04/5G-Range_D2.1_Application_Requirement_Report_v1.pdf

[11] *Measurements of Extreme Rural Scenarios*, document R1-166599, Telstra, Ericsson, Aug. 2016.

[12] *Study on Channel Model for Frequencies from 0.5 to 100 GHz*, document TR 38.901, Release 14, 3GPP, Mar. 2017.

[13] A. M. Pessoa, B. Sokal, C. F. M. E. Silva, T. F. Maciel, A. L. F. de Almeida, D. A. Sousa, Y. C. B. Silva, and F. R. P. Cavalcanti, "CDL-based channel model for 5G MIMO systems in remote rural areas," in *Proc. 16th Int. Symp. Wireless Commun. Syst. (ISWCS)*, Aug. 2019, pp. 21–26.

[14] ITU-R, "Guidelines for evaluation of radio interface technologies for IMT-2020," Tech. Rep. ITU-R M.2412-0, Oct. 2017. [Online]. Available: https://www.itu.int/pub/R-REP-M.2412-2017

[15] P. Kyosti *et al.*, "ST-4-027756 WINNER II D1.1.2 v1.2: WINNER II channel models," Tech. Rep., 2007. [Online]. Available: https://www.cept.org/files/8339/winner2%20-%20final%20report.pdf

[16] S. Jaeckel, L. Raschkowski, L. Thiele, F. Burkhardt, and E. Eberlein, "QuaDRiGa—Quasi deterministic radio channel generator, user manual and documentation," Fraunhofer Heinrich Hertz Inst., Berlin, Germany, Tech. Rep. V2.0.0, 2017.

[17] H. Asplund, A. A. Glazunov, A. F. Molisch, K. I. Pedersen, and M. Steinbauer, "The COST 259 directional channel model—Part II: Macrocells," *IEEE Trans. Wireless Commun.*, vol. 5, no. 12, pp. 3434–3450, Dec. 2006.

[18] H. Jiang, Z. Zhang, J. Dang, and L. Wu, "A novel 3-D massive MIMO channel model for vehicle-to-vehicle communication environments," *IEEE Trans. Commun.*, vol. 66, no. 1, pp. 79–90, Jan. 2018.

[19] H. Jiang, Z. Zhang, L. Wu, J. Dang, and G. Gui, "A 3-D non-stationary wideband geometry-based channel model for MIMO vehicle-to-vehicle communications in tunnel environments," *IEEE Trans. Veh. Technol.*, vol. 68, no. 7, pp. 6257–6271, Jul. 2019.

[20] K. Haneda *et al.*, "Measurement results and final mmMAGIC channel models," Millimetre-Wave Based Mobile Radio Access Network for Fifth Generation Integrated Communications (mmMAGIC), Deliverable D2.2 v2, May 2017. [Online]. Available: https://bscw.5g-mmmagic.eu/pub/bscw.cgi/d202656/mmMAGIC_D2-2.pdf

[21] V. Nurmela *et al.*, "METIS channel models," Mobile and Wireless Communications Enablers for the Twenty-twenty Information Society (METIS), Deliverable D1.4 v1.0, Jul. 2015. [Online]. Available: https://metis2020.com/wp-content/uploads/deliverables/METIS_D1.4_v1.0.pdf

[22] C.-X. Wang, J. Bian, J. Sun, W. Zhang, and M. Zhang, "A survey of 5G channel measurements and models," *IEEE Commun. Surveys Tuts.*, vol. 20, no. 4, pp. 3142–3168, Aug. 2018.

[23] *Path Loss Model for Extreme Rural Scenario*, document R1-167452, Telstra, Ericsson, Aug. 2016.

[24] P. L. Rice, "Transmission loss predictions for tropospheric communication circuits," U.S. Nat. Bureau Standards, Washington, DC, USA, Tech. Rep., 1967.

[25] *Method for Point-to-Area Predictions for Terrestrial Services in the Frequency Range 30 MHz to 3000 MHz*, document Rec. ITU-R P.1546-5, Sep. 2013.

[26] L. Gavrilovska, P. Latkoski, V. Atanasovski, R. Prasad, A. Mihovska, O. Fratu, and P. Lazaridis, "Radio spectrum: Evaluation approaches, coexistence issues and monitoring," *Comput. Netw.*, vol. 121, pp. 1–12, Jul. 2017.

[27] *Channel Model for Extreme Rural Scenario*, document R1-167451, Telstra, Ericsson, Aug. 2016.

[28] C. Oestges, B. Clerckx, M. Guillaud, and M. Debbah, "Dual-polarized wireless communications: From propagation models to system performance evaluation," *IEEE Trans. Wireless Commun.*, vol. 7, no. 10, pp. 4019–4031, Oct. 2008.

[29] M. Coldrey, "Modeling and capacity of polarized MIMO channels," in *Proc. IEEE Veh. Technol. Conf. (VTC Spring)*, May 2008, pp. 440–444.

[30] S. Ogawa and F. Ono, "STBC-MIMO network coding with dual polarization antennas," in *Proc. 20th Int. Conf. Comput. Commun. Netw. (ICCCN)*, Jul. 2011, pp. 1–6.

[31] B. J. Wysocki, T. A. Wysocki, and S. S. Adams, "On an orthogonal space-time-polarization block code," *J. Commun.*, vol. 4, no. 1, pp. 20–25, Feb. 2009.

[32] J.-K. Hong, "Performance analysis of dual-polarized massive MIMO system with human-care IoT devices for cellular networks," *J. Sensors*, vol. 2018, pp. 1–8, Jan. 2018.

[33] O. Jo, J.-J. Kim, J. Yoon, D. Choi, and W. Hong, "Exploitation of dual-polarization diversity for 5G millimeter-wave MIMO beamforming systems," *IEEE Trans. Antennas Propag.*, vol. 65, no. 12, pp. 6646–6655, Dec. 2017.

[34] A. W. Bowman, "An alternative method of cross-validation for the smoothing of density estimates," *Biometrika*, vol. 71, no. 2, pp. 353–360, Aug. 1984.

[35] *Public Safety Broadband High Power User Equipment (UE) for Band 14*, document TR 36.837, Release 11, 3GPP, Dec. 2012.

[36] D. Potts, G. Steidl, and M. Tasche, "Fast Fourier transforms for nonequispaced data: A tutorial," in *Modern Sampling Theory. Applied and Numerical Harmonic Analysis*, J. J. Benedetto and P. J. S. G. Ferreira, Eds. Boston, MA, USA: Birkhäuser, 2001. [Online]. Available: https://link.springer.com/chapter/10.1007/978-1-4612-0143-4_12#citeas, doi: 10.1007/978-1-4612-0143-4_12.

[37] A. F. Molisch and M. Steinbauer, "Condensed parameters for characterizing wideband mobile radio channels," *Int. J. Wireless Inf. Netw.*, vol. 6, no. 3, pp. 133–154, Jul. 1999.
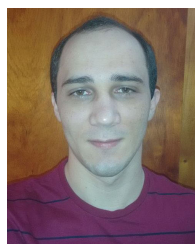
ALEXANDRE MATOS PESSOA (Student Member, IEEE) received the B.Sc. and M.Sc. degrees in computer engineering from the Federal University of Ceará (UFC), Sobral, Brazil, in 2015 and 2017, respectively, where he is currently pursuing the D.Sc. degree in teleinformatics with emphasis in systems and communication networks. Since 2014, he has been a Collaborator and a Researcher with the Wireless Telecom Research Group (GTEL), UFC, where he works in the Project 5G-Remote Area Access Network for 5G Generation (RANGE) in cooperation with universities/institutes from Brazil and Europe. His research interests include radio resource allocation for spectrum sensing techniques and channel modeling.
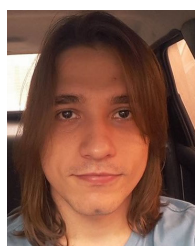
BRUNO SOKAL (Student Member, IEEE) received the B.Sc. degree in telecommunications engineering from the Federal Institution of Science, Education and Technology of Ceará (IFCE), Fortaleza, Brazil, in 2015, and the M.Sc. degree in teleinformatics engineering from the Federal University of Ceará (UFC), Fortaleza, in 2017, where he is currently pursuing the D.Sc. degree in teleinformatics engineering with the emphasis in signal processing in telecommunications. Since 2017, he has been a Collaborator and a Researcher with the Wireless Telecom Research Group (GTEL), UFC, where he also works in the Project 5G-Remote Area Access Network for Fifth Generation (RANGE).

CARLOS F. M. E SILVA (Member, IEEE) received the Diploma and M.Sc. degrees in electronics and telecommunications engineering from the University of Aveiro (UA), Portugal, in 2005 and 2010, respectively, and the Ph.D. degree in teleinformatics engineering from the Federal University of Ceará (UFC), Brazil, in 2015. Since 2006, he has been a Researcher in several European projects, such as WINNER II (system requirements for beyond third generation wireless networks), FUTON (RRM for wireless and optical networks), and COGEU (cognitive radio systems for efficient use and sharing of TVWS in the European context). He holds a postdoctoral position with the Wireless Telecom Research Group (GTEL), Brazil, where he manages GTEL's team with the European-Brazilian Project FUTEBOL and also works in cooperation projects with Ericsson Research. His main research interests include spectrum usage optimization, TV white spaces, licensed shared access, the Internet of Things, device-to-device communications, testbed experimentation, and architectural aspects of the future 5G networks.

TARCISIO FERREIRA MACIEL received the B.Sc. and M.Sc. degrees in electrical engineering from the Federal University of Ceará (UFC), in 2002 and 2004, respectively, and the Dr.-Ing. degree in electrical engineering from the Technische Universität Darmstadt (TUD), Germany, in 2008. Since 2001, he has been actively participated in several projects in a technical and scientific cooperation with the Wireless Telecom Research Group (GTEL), UFC, and Ericsson Research. From 2005 to 2008, he was a Research Assistant with the Communications Engineering Laboratory, TUD. Since 2008, he has been a member with the Post-Graduation Program in teleinformatics engineering, UFC. In 2009, he was a Professor of computer engineering with UFC, Sobral. Since 2010, he has been a Professor with the Center of Technology, UFC. His research interests include radio resource management, numerical optimization, and multiuser/multiantenna communications.

ANDRÉ L. F. DE ALMEIDA (Senior Member, IEEE) received the double Ph.D. degrees in sciences and teleinformatics engineering from the University of Nice Sophia Antipolis, France, and the Federal University of Ceará, Fortaleza, Brazil, in 2007. From 2007 to 2008, he held a one-year teaching position at the University of Nice Sophia Antipolis. He is currently an Associate Professor with the Department of Teleinformatics Engineering, Federal University of Ceará. He was awarded multiple times Visiting Professor positions at the University of Nice Sophia Antipolis. His research interests include the topics of channel estimation, sensor array processing, and multi-antenna systems. An important part of his research has been devoted to multilinear algebra and tensor decompositions with applications to communications and signal processing. He is a member of the Sensor Array and Multichannel (SAM) Technical Committee of the IEEE Signal Processing Society (SPS) and the EURASIP Signal Processing for Multi-Sensor Systems Technical Area Committee (SPMuS–TAC). He is a Research Fellow of the CNPq (the Brazilian National Council for Scientific and Technological Development). In January 2018, he was elected as an Affiliate Member of the Brazilian Academy of Sciences. He was the General Co-Chair of the IEEE CAMSAP'2017 Workshop and served as the Technical Co-Chair of the Symposium on Tensor Methods for Signal Processing and Machine Learning at IEEE GlobalSIP 2018 and 2019 editions. He also served as the Technical Co-Chair of the IEEE SAM 2020 Workshop, Hangzhou, China, and is the General Co-Chair of the IEEE CAMSAP 2021 Workshop. He served as an Associate Editor for the IEEE Transactions on Signal Processing from 2012 to 2016. He currently serves as an Associate Editor for the IEEE Signal Processing Letters.

FRANCISCO RODRIGO PORTO CAVALCANTI (Member, IEEE) received the B.Sc. and M.Sc. degrees in electrical engineering from the Federal University of Ceará (UFC), Fortaleza, Brazil, in 1994 and 1996, respectively, and the D.Sc. degree in electrical engineering from the State University of Campinas, São Paulo, Brazil, in 1999. In 2000, he founded and directed the Research Laboratory, Wireless Telecom Research Group (GTEL), Fortaleza, which focuses on the advancement of wireless telecommunications technologies, where he manages a Program of research projects in wireless communications sponsored by the Ericsson Innovation Center, Brazil, and Ericsson Research, Sweden. He joined UFC, where he is currently an Associate Professor and holds the Wireless Communications Chair with the Department of Teleinformatics Engineering. He is also a Distinguished Researcher with the Brazilian Scientific and Technological Development Council for the technology development and innovation record. He has produced a varied body of work, including two edited books, conference papers and journal articles, international patents, and computer software dealing with subjects, such as radio resource allocation, cross-layer algorithms, quality of service provisioning, radio transceiver architectures, signal processing, and project management. He received the Leadership and Management Professional Certificate from the Massachusetts Institute of Technology, Cambridge.

● ● ●